Chinese Chemical Letters 37 (2026) 111389

Contents lists available at ScienceDirect

Chinese Chemical Letters

journal homepage: www.elsevier.com/locate/cclet

Covalent organic frameworks: An emerging class of piezoelectric materials for mechanical energy transfer application

Lijiang Guan, Danyal Mehdi, Haoxiang Li*, Fei Chen, Shangbin Jin*

State Key Laboratory of Fluorine & Nitrogen Chemicals, School of Chemical Engineering and Technology, Xi'an Jiaotong University, Xi'an 710049, China

ARTICLE INFO

Article history:
Received 22 February 2025
Revised 22 May 2025
Accepted 28 May 2025
Available online 28 May 2025

Keywords:
Covalent organic frameworks
Piezoelectric effect
Piezocatalysis
Piezoelectric nanogenerator
Structural transformation

ABSTRACT

Piezoelectric materials can efficiently convert widely available mechanical energy to usable electrical energy or chemical energy, which represent a type of promising sustainable materials and is worth being extensively explored. Covalent organic frameworks (COFs), with their finely tunable structures and properties, have emerged as exciting materials for piezoelectric applications. This review aims to discuss the strategy for enhanced piezoelectric properties of COFs and the applications of COFs in the piezoelectric field, including piezocatalysis and piezoelectric nanogenerators. Then, the effect of pressure on the structure of COFs is introduced, which may provide new perspectives for the design of COFs in piezoelectricity. The review concludes that COFs offer a versatile platform for developing advanced piezoelectric materials, with potential in wide range of applications. The insights provided in this review are hoped to guide the direction of future research in the field of COF-based piezoelectric materials.

© 2026 Published by Elsevier B.V. on behalf of Chinese Chemical Society and Institute of Materia Medica, Chinese Academy of Medical Sciences.

1. Introduction

Mechanical energy is a fundamental and widely available form of energy and its capture, conversion and efficient use is of vital importance in overcoming energy shortages and mitigating environmental challenges. First discovered in 1880 [1], some materials could conduct an electrical potential under mechanical stress. This conversion of the mechanical energy into the electrical energy is referred to as the piezoelectric effect [2–4]. Microscopically, when a material undergoes deformation due to an applied mechanical force, the positions of its constituent atoms in the crystal lattice are altered, resulting in a redistribution of charge (Fig. 1a). This displacement of charges results in the formation of dipole moments and the generation of a piezoelectric potential [5,6]. In theory, the piezoelectric effect can only be found in non-centrosymmetric materials [4,5]. Of the 32 crystal classes, 21 crystal classes are non-centrosymmetric, 10 of which (1, 2, *m*, *mm*2, 3, 3*m*, 4, 4*mm*, 6, 6*mm*) are polar and capable of spontaneous polarization and other 10 of which (222, $\bar{4}$, 422, $\bar{4}2m$, 32, $\bar{6}$, 622, $\bar{6}m2$, 23, $\bar{4}3m$) can produce a dipole under an external force. The other one (432) of these 21 crystal classes is non-centrosymmetric but still show symmetry, thus does not exhibit the piezoelectric effect. Over the past few decades, a wide diversity of piezoelectric materials has been identified, such as quartz [7], ZnO [8], MoS_2 [9], $BaTiO_3$ [10], $BiOIO_3$ [11], polyvinylidene fluoride (PVDF) (Fig. 1b) [12]. Recently, other emerging crystalline materials, such as metal-organic frameworks (MOFs) [13,14] and graphitic carbon nitride (g-C_3N_4) [15,16], have demonstrated significant piezoelectric properties (Figs. 1c and d). Currently, piezoelectric materials are widely used in many fields like sensing [17,18], energy harvesting [19], medical devices [20,21], acoustic devices [22] and so on due to their efficient conversion ability between mechanical stress and electrical signals. With the ongoing advancement of technology, piezoelectric materials are increasingly being explored for use in emerging domains, such as smart materials [23], catalysis [24,25] and electronic devices [26].

In 2005, Yaghi *et al.* presented a pioneering study on the porous organic frameworks, which are linked by reversible covalent bonds [27]. They were the first samples of what came to be known as covalent organic frameworks (COFs) that combine π-conjugated system with a permanent porous skeleton [28–30]. The COFs provide a number of available functional sites due to inherent porosity and large surface area, which facilitate the adsorption or mass transfer of guest molecules. And, the precisely tunable structures give COFs specific size and shape of pores. Furthermore, the conjugated skeleton in COFs promotes efficient charge transfer. Therefore, COFs have become attractive porous materials and have been used in many fields, such as separations, gas adsorption, catalysis, sensing and energy storage [31]. In 2017, Yin *et al.* used first-principles calculations to reveal the piezoelectricity of monolayer COFs for first time [32]. The flexibility in building blocks of

* Corresponding authors.
E-mail addresses: lihaoxiang@xjtu.edu.cn (H. Li), shangbin@xjtu.edu.cn (S. Jin).

https://doi.org/10.1016/j.cclet.2025.111389
1001-8417/© 2026 Published by Elsevier B.V. on behalf of Chinese Chemical Society and Institute of Materia Medica, Chinese Academy of Medical Sciences.

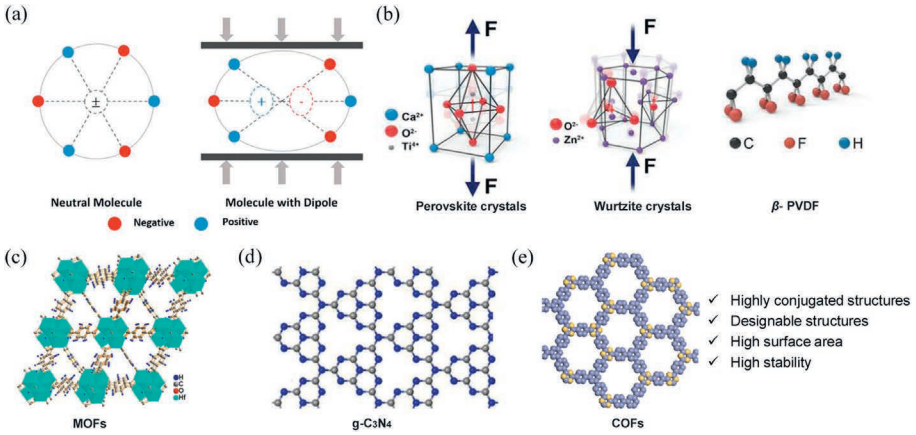


Fig. 1. (a) Mechanism of piezoelectric properties. Reproduced with permission [6]. Copyright 2022, IOP Publishing. (b) Some classic piezoelectric materials such as perovskite crystals (represented by $CaTiO_3$), wurtzite crystals (represented by ZnO) and PVDF. Reproduced with permission [5]. Copyright 2020, the John Wily and Sons. (c) Piezoelectric MOFs materials (represented by UiO-66(Hf)). Reproduced with permission [13]. Copyright 2019, American Chemical Society. (d) Piezoelectric g-C_3N_4 materials. Reproduced with permission [15]. Copyright 2014, Springer Nature. (e) COFs (represented by covalent triazine frameworks) as piezoelectric materials.

COFs offers extensive opportunities for structural optimization, positioning COFs as promising candidates for piezoelectric materials (Fig. 1e). COFs could demonstrate unique advantages over conventional piezoelectric materials originate from their highly designable molecular structures and porous properties. The modular construction of COFs allows the precise tuning of piezoelectric properties by incorporation of polar-functionalized monomers, using non-symmetric building blocks or employing topological structure design to realize non-centrosymmetric crystal structures [31]. And, the programmable functionalization capability of COFs permits targeted modification for diverse piezoelectric applications. Furthermore, under mechanical stress, the nanopores of COF are prone to deformation resulting from an increase in local stress intensity [33], but also provides confined spaces for loading functional guests to enhance piezoelectric performance through interfacial polarization effects. However, as emerging materials, research on the piezoelectric properties of COFs is still in its infancy, and further investigation is necessary to understand their full potential in this area.

In recent years, COFs have been presented as a promising platform, exhibiting excellent piezoelectric catalytic activity [34] and effectively functioning as piezoelectric nanogenerators (PENGs) [35]. These developments highlight the significant potential of COFs as advanced materials for piezoelectric applications.

It is worth noting that although numerous comprehensive reviews have extensively covered the synthesis, structural design, and various applications of COFs [29,31,36], as well as various other piezoelectric materials [24,37–40], there is still a lack of dedicated reviews devoted to the research of COFs in terms of piezoelectric properties. Therefore, in this review, we focus on summarizing the strategy for improving piezoelectric properties of COFs. Then, the progress on COFs for piezocatalysis and piezoelectric nanogenerators is first presented. We also introduce the results on the structural evolution of COFs under high pressure, hoping to provide a way to reveal the structure-property relationship in piezoelectric processes and to provide guidance for the design of target piezoelectric COFs.

2. Strategy for enhanced piezoelectric properties of COFs

2.1. Structural design

COFs have a remarkable structural designability, offering great potential for piezoelectric performance enhancement. Recently, Liu *et al.* have synthesized EA-COF and employed piezoresponse force microscopy (PFM) to confirm the piezoelectric properties of the EA-COF (Fig. 2) [41]. As illustrated in Fig. 2b, upon application of a voltage, the EA-COF exhibited a distinct peak at 300 kHz, with the amplitude showing a linear correlation to the applied voltage (Fig. 2c). The phase changes, observed in the piezoresponse phase hysteresis loops, was approximately 170° over a sweep bias range of −5∼5 V (Fig. 2d). Furthermore, the butterfly amplitude loop further validated its piezoelectric behavior (Fig. 2e). The piezoelectric coefficient (d_{33}) of the EA-COF was 319.20 pm/V. The density functional theory (DFT) calculations further demonstrate that the piezoelectricity of EA-COF is given by the in-plane polarization of Tp subunits.

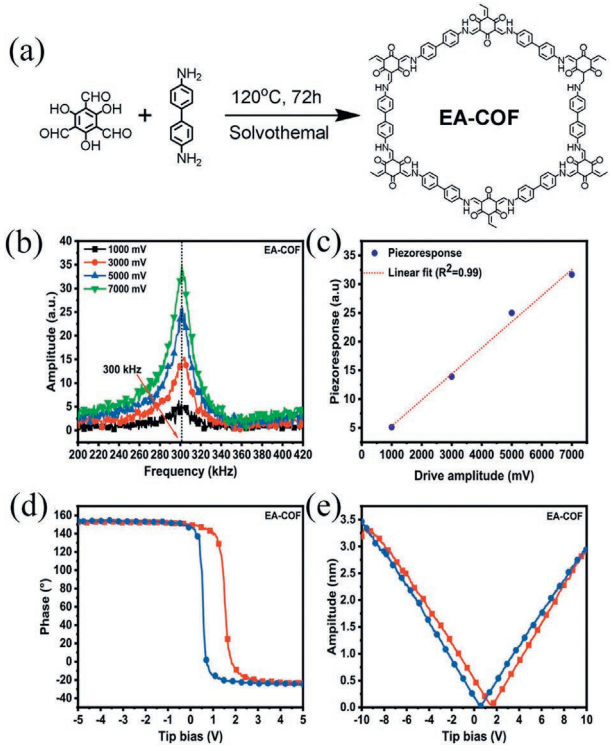


Fig. 2. (a) Synthesis of EA-COF. (b) EA-COF resonance peaks for different applied voltages. (c) Linear relationship between operating voltage and EA-COF amplitude. (d, e) The EA-COF displacement voltage and phase curves. Reproduced with permission [41]. Copyright 2024, American Chemical Society.

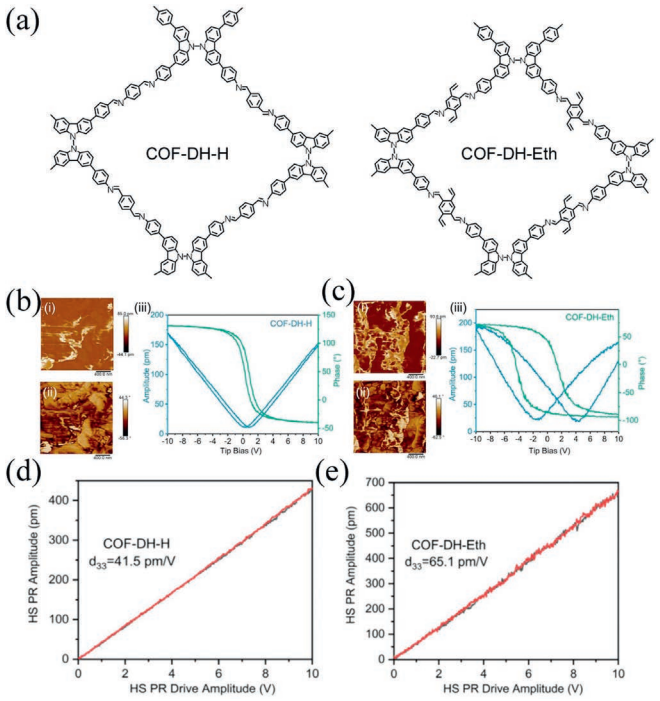


Fig. 3. (a) Synthesis of COF-DH–H and COF-DH-Eth. The PFM images for (i) amplitude, (ii) phase and (iii) the phase curves and amplitude butterfly loop of (b) COF-DH–H and (c) COF-DH-Eth. The relationship between piezoresponse and applied voltage for (d) COF-DH–H and (e) COF-DH-Eth. Reproduced with permission [42]. Copyright 2024, the John Wily and Sons.

Han and colleagues synthesized two bicarbazole-based COFs (Cz-COFs), namely COF-DH–H and COF-DH-Eth, featuring distinct functional groups (Fig. 3) [42]. These two COFs were identified as the *C*2 space group, a non-centrosymmetric crystal structure. With an external voltage, both COF-DH–H and COF-DH-Eth exhibited a characteristic butterfly-shaped amplitude loop and a 180° phase changes, indicating their typical piezoelectric behavior (Figs. 3b and c). Furthermore, the piezoelectric coefficient (d_{33}) of COF-DH–H and COF-DH-Eth were evaluated to be approximately 41.5 and 65.1 pm/V (Figs. 3d and e), respectively, surpassing the d_{33} values of commercial PVDF (~20–35 pm/V) [43]. These findings highlight the pronounced piezoelectric responses of the two Cz-COFs. Additionally, the bifluorenylidene-based COF (COF-BFTB-H) was also found to possess good piezoelectric properties with a piezoelectric coefficient of 25.3 pm/V. This indicates that twisted monomers, such as bicarbazole and bifluorenylidene molecules, can effectively break the symmetry of COFs, imparting piezoelectric properties to these COFs.

Zhang *et al.* developed two distinct two-dimensional COFs, designated CityU-13 and CityU-14, attributed to the *P*1 space group (Fig. 4) [35]. These COFs exhibit piezoelectric properties through the incorporation of fluorinated alkyl chains (Figs. 4b and c). CityU-13 and CityU-14 exhibit exceptional piezoelectric performance, with piezoelectric coefficients of 20.9 pC/N and 18.9 pC/N, respectively, measured by the *quasi*-static method. The high electronegativity of fluorine atoms induces strong polarization of the C-F bonds, leading to a considerable dipole moment. In addition, the ordered nanostructure of the COFs facilitates *in situ* orientation of methylene (-CH_2) and difluoromethylene (-CF_2) groups within the fluorinated alkyl chains, resulting in permanent polarization. Therefore, the introduction of fluorinated alkyl chains imparts asymmetry structures and intrinsic polarizability to the COFs, thus contributing to the significant piezoelectric response.

Maji *et al.* synthesized two imide-linked COFs, namely TAPA-PDA and TAPB-PDA (Fig. 5a) [44]. The TAPA building block has

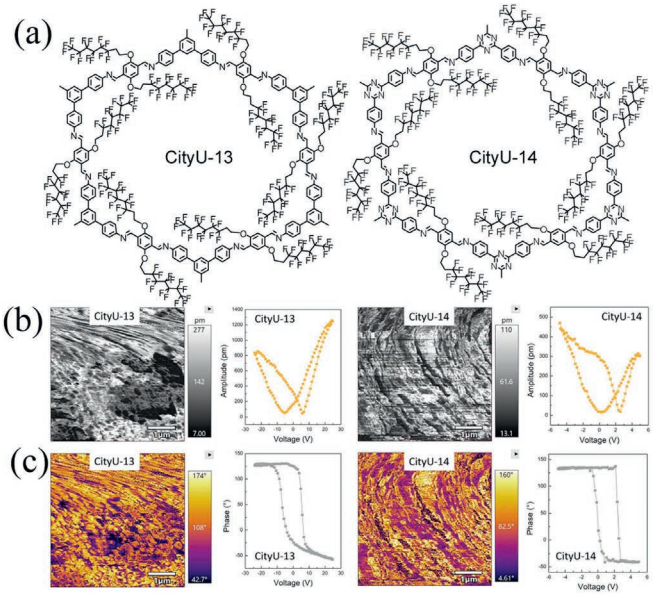


Fig. 4. (a) Chemical structures of CityU-13 and CityU-14. (b) Vertical PFM amplitudes and corresponding amplitude butterfly loops of CityU-13 and CityU-14. (c) PFM phase images and corresponding piezoresponse phase hysteresis loops of CityU-13 and CityU-14. Reproduced with permission [35]. Copyright 2024, the John Wily and Sons.

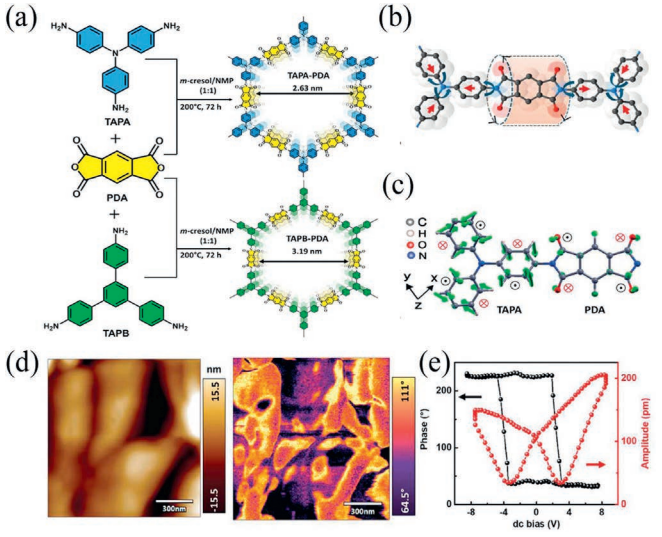


Fig. 5. (a) Synthesis of TAPA-PDA and TAPB-PDA. (b) Schematic diagram of molecular distortion in TAPA-PDA. (c) Structural changes in TAPB-PDA. (d) Topography image and phase image of TAPA-PDA and (e) the phase curves and amplitude butterfly loop of TAPA-PDA. Reproduced with permission [44]. Copyright 2025, the John Wily and Sons.

a propeller-like motif with breaking symmetry by twisting and tilting (Fig. 5b), whereas the TAPB does not have this attribute (Fig. 5c). As a result, TAPA-PDA exhibits the non-centrosymmetric space group *P*622, while the TAPB-PDA adopts the symmetric space group $P\bar{3}1m$. As direct evidence, the PFM and Kelvin probe force microscopy (KPFM) measurements reveal that TAPA-PDA exhibits a good piezoelectric response (Figs. 5d and e).

2.2. Defect engineering

Defect engineering could be a powerful strategy to break the symmetry of COFs. Qiu *et al.* successfully synthesized COF@ZnO heterojunctions by *in situ* preparation of COFs on the surface of ZnO [45]. This approach leverages the dynamically reversible na-

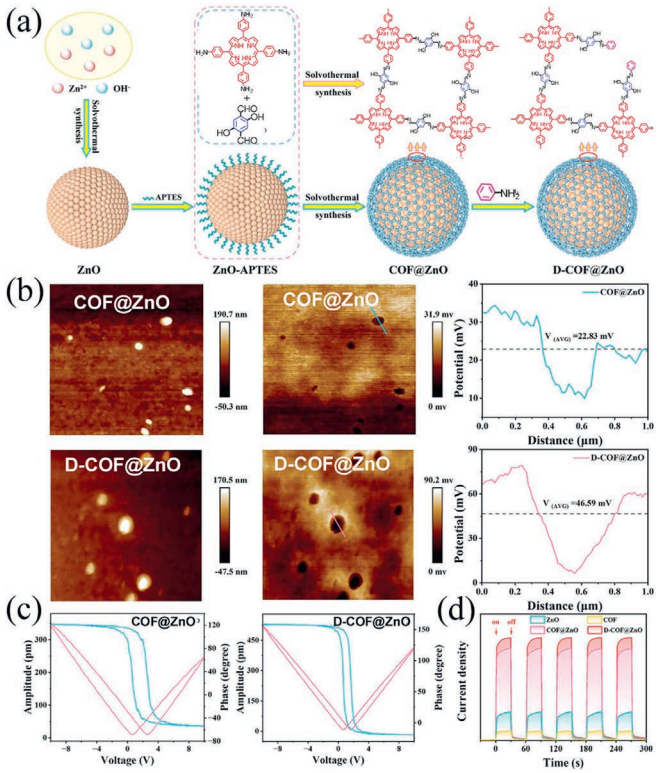


Fig. 6. (a) Synthetic procedure for defect heterogeneous engineering D-COF@ZnO. (b) The topographic images, the surface KPFM potential images and surface piezoelectric potentials of COF@ZnO and D-COF@ZnO. (c) The phase hysteresis curves and amplitude butterfly-shaped loop of COF@ZnO and D-COF@ZnO. (d) Transient piezoelectric current curves. Reproduced with permission [45]. Copyright 2024, the John Wily and Sons.

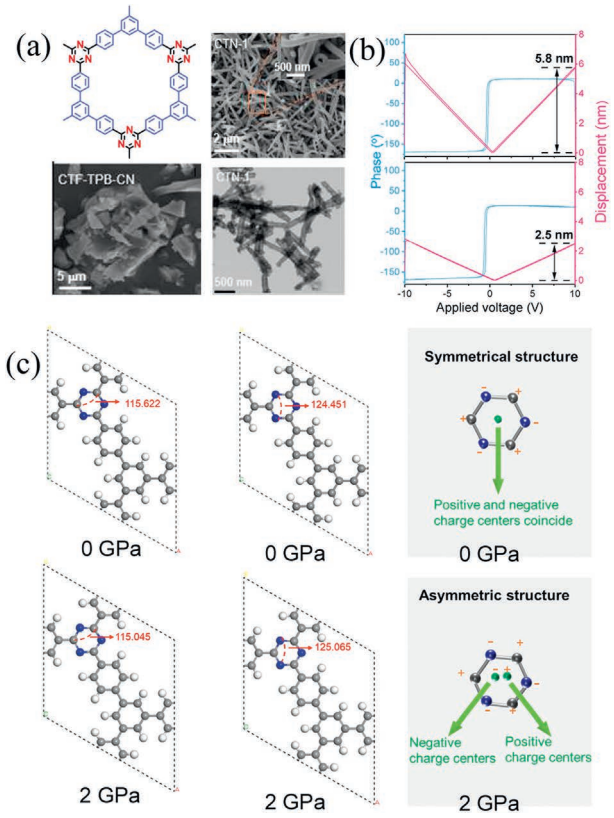


Fig. 7. (a) Chemical structure, SEM and TEM images of CTN-1, CTF-TPB-CN was used as a comparison sample. (b) The phase hysteresis curves and amplitude butterfly-shaped loop of CTFs. (c) The bond angles of the triazine rings without or with pressure. Reproduced with permission [34]. Copyright 2024, the John Wily and Sons.

ture of imine bonding to introduce aniline molecules to create defects (Fig. 6). The introduction of structural defects affects the local atomic coordination within the COF, leading to lattice strain and symmetry reduction. Consequently, this symmetry-breaking effect enhances the polarization of the material, resulting in a piezoelectric effect. The PFM and KPFM measurements reveal that the defect-engineered COF@ZnO (denoted as D-COF@ZnO) exhibits a significantly higher piezoelectric response and larger surface piezoelectric potential compared to the unmodified COF@ZnO (Figs. 6b and c). Under ultrasonic treatment, D-COF@ZnO demonstrates notably stronger current responses than COF@ZnO (Fig. 6d).

2.3. Morphology control

It was also found that morphology plays a critical role in enhancing the piezoelectric response. Covalent triazine frameworks (CTFs), a subclass of COFs, are characterized by the robust linkage of the triazine rings, which gives them superior structural stability compared to many other COFs. The highly conjugated and nitrogen-rich frameworks of CTFs contribute to their enhanced polarity.

To improve the piezoelectricity of CTFs, Jin *et al.* developed the bottom-up synthesis of covalent triazine nanotube (CTN-1), which exhibits a one-dimensional tubular morphology (Fig. 7a) and demonstrates better mechanical stimuli response than CTF-TPB-CN with unrolling nanosheets morphology according to PFM results (Fig. 7b) [34]. Based on DFT theoretical calculations, the authors propose the origin of the piezoelectric properties of CTFs, revealing that pressure leads to deformation of the bond angles of the triazine ring, which creates an asymmetry and generates a pronounced dipole (Fig. 7c).

2.4. Anchoring metals atoms

Anchoring metals in the framework of COFs is also a promising strategy to improve asymmetry. Zhu and Xia *et al.* successfully anchored the antimony (Sb) atom to the bipyridine subunits of TpBpy-COF in the situation of Sb-N coordination *via* 5p-2p orbitals hybridization, denoted as SASb-TpBpy-COF (SA: single-atom) (Fig. 8a) [46]. This strategy can greatly improve the asymmetry within the framework by changing the local electronic polarization, significantly improving the piezoelectric properties. The piezoelectric response potentials generated by SASb-TpBpy-COF and TpBpy-COF were determined to be 21.14 and 3.33 mV, respectively, indicating a marked increase in the piezoelectric activity (Figs. 8b and c). The butterfly shapes of both SASb-TpBpy-COF and TpBpy-COF indicated good piezoelectric response (Figs. 8d and e). The piezoelectric coefficients of SASb-TpBpy-COF (Sb: 0.72 wt%) and TpBpy-COF are ~287.6 and 126.3 pm/V, respectively, showing significantly enhanced piezoelectric properties after anchoring the metal. The authors investigated the dipole moments of these two COFs by theoretical calculations. The results show that the dipole moment of SASb-TpBpy-COF is 0.016 D, while TpBpy-COF has almost no dipole, confirming that the polarization is improved by anchoring the Sb.

3. Piezoelectric applications of COFs

3.1. COFs for piezocatalysis

In 2010, Hou *et al.* reported the overall water splitting for the production of H_2 and O_2 under ultrasonic irradiation, employing fibrous ZnO and dendritic $BaTiO_3$ as catalysts [47]. This pioneer-

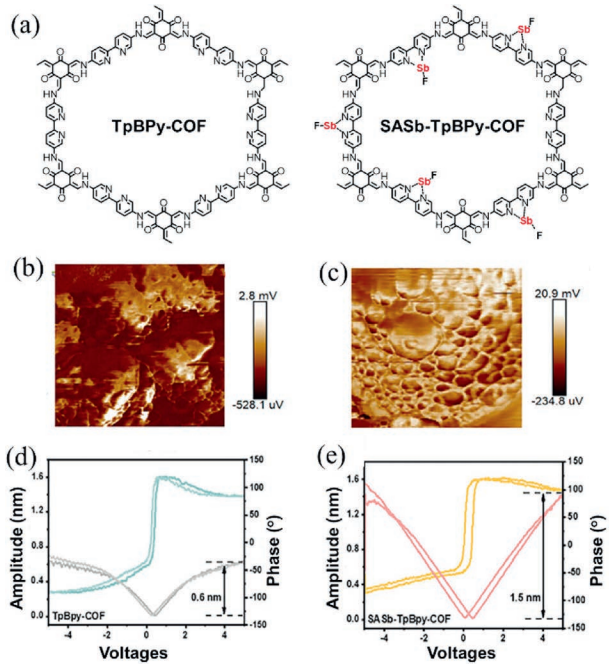


Fig. 8. (a) Chemical structures of COFs. Piezoelectric properties mapping images of (b) TpBpy-COF and (c) SASb-TpBpy-COF. The phase curves and amplitude butterfly loop of (d) TpBpy-COF and (e) SASb-TpBpy-COF. Reproduced with permission [46]. Copyright 2025, the John Wily and Sons.

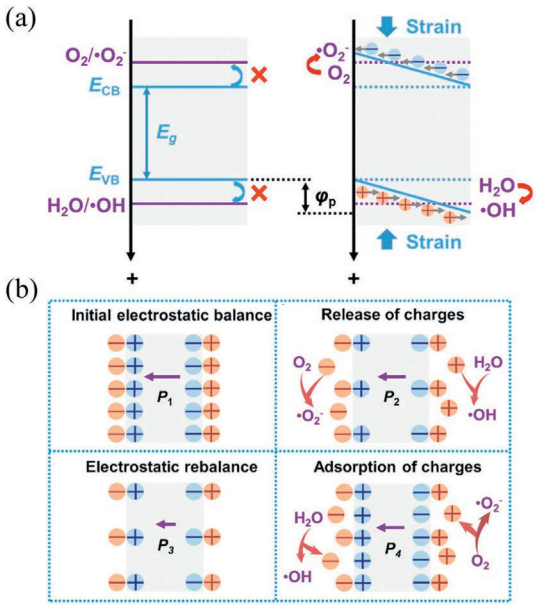


Fig. 9. (a) Schematic description of the energy band theory in the piezocatalysis process. Reproduced with permission [25]. (b) Schematic description of the screening charge effect in the piezocatalysis process. Reproduced with permission [25]. Copyright 2023, Elsevier.

ing work is recognized as the beginning of research in the field of piezocatalysis. Over the past decade, piezocatalysis has become a significant approach in various areas, such as pollutant degradation [24], water splitting [48–50], H_2O_2 production [51–53], CO_2 reduction [54,55], N_2 fixation [56,57] and synthesis of high-value chemicals [58–60].

COFs are emerging as promising semiconductor materials, showing significant potential in photocatalysis and electrocatalysis [61–63]. However, their piezocatalytic performance has only recently begun to be investigated. Compared to conventional inorganic piezoelectric materials, the inherent porosity of COFs increases the number of active sites that are available for catalytic reactions [52]. Furthermore, COFs exhibit superior stability compared to MOFs, making them more tolerant to operating conditions [64]. In addition, COFs generally have a higher degree of conjugation and greater structural tunability compared to g-C_3N_4 [65]. These advantages would make COFs as highly promising candidates for advancing piezocatalysis.

3.1.1. The mechanism of piezocatalysis

Despite the rapid advancements in the field, the mechanism of piezocatalysis has not been fully elucidated. The proposed theories were used to explain piezocatalysis, including energy band theory and the screening charge effect [3].

Inspired by photocatalysis, the energy band theory posits that external stimuli promote electrons in piezocatalysts to migrate, thereby initiating redox reactions [66]. The proposed mechanism suggests that during piezocatalysis, external forces - such as the high pressures generated by the cavitation effect of ultrasound - act as a driving force to facilitate electronic excitation [67]. When the piezocatalyst undergoing mechanical deformation, a dipole moment is generated within the material, resulting in the creation of an internal piezoelectric potential field. The piezo-potential field is critical for catalytic activity, as it can modulate the electronic properties of the material and influence the chemical reactions occurring at its surface [25]. More specifically, the piezo-potential field would induce bending of the energy band of the piezoelectric materials, making catalytic reactions thermodynamically favorable (Fig. 9a). In addition, the presence of the piezo-potential field could increase the efficiency of charge separation where it can participate more effectively in the reaction.

The screening charge effect mainly involves the piezo-potential and the charge screening behavior of the catalyst surface [3]. Owing to the polarization effect of piezoelectric materials, the charges are stored on the surface of the piezocatalyst, which allows the adsorption of an external charge from the solvent. Upon the application of external stimuli, the charge equilibrium at the catalyst surface is disrupted, which leads to a reduction in polarization capacity and the partial release of adsorbed external charges, thereby triggering redox reactions (Fig. 9b). Once the external force is removed, the polarization would be restored, and the charges from the solvent are re-adsorbed onto the catalyst surface. Typically, in an aqueous environment, OH^-, H_2O and H^+ may be the primary screening species [3]. However, the electrons involved in reduction reactions may originate from the dissociation of water or hydroxide ions. The theory highlights the crucial role of the piezo-potential as the driving force for redox reactions, which would determine the catalytic activity. The screening charge effect is a key difference from the energy band theory, in which the charge for a redox reaction is assumed to be charges from an external system, instead of from intrinsic charge carriers within the material.

Both mechanisms have been proposed to explain the experimental observations. However, they remain a subject of ongoing debate. Recently, comparing the catalytic degradation have suggested that these two mechanisms are likely to coexist during piezocatalysis [68]. Zhu *et al.* investigated the intermediate products involved in the piezocatalytic H_2O_2 production by a BOB-OV piezocatalyst using *in situ* electron paramagnetic resonance (EPR). The results were compared with those from photocatalysis and electrocatalysis, revealing that the piezocatalytic process shows a greater similarity to photocatalysis [69].

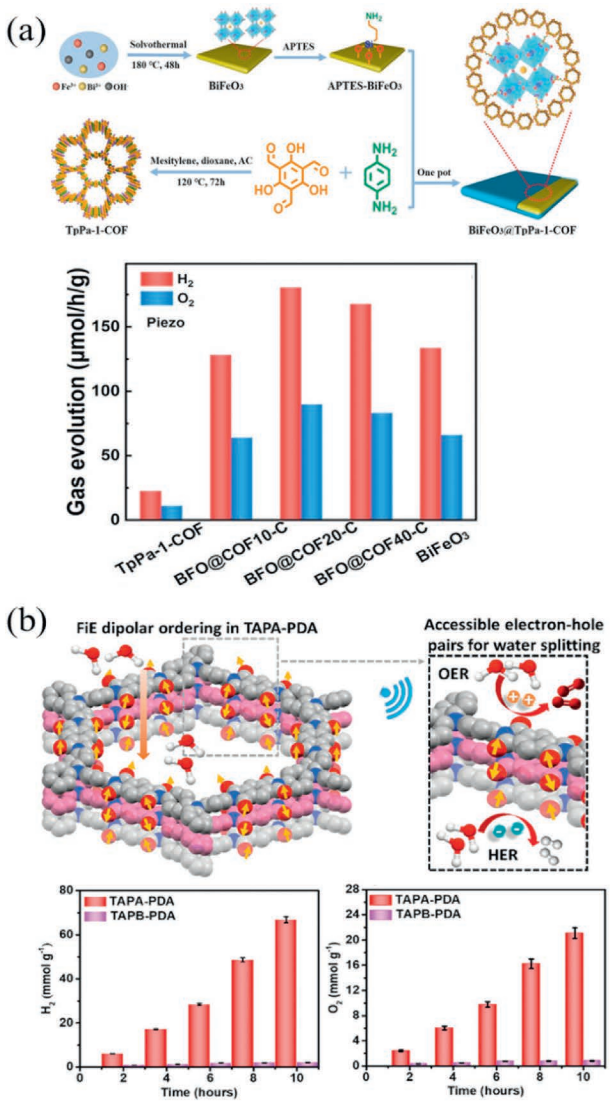


Fig. 10. (a) Scheme of the synthesis procedure of the $BiFeO_3$@TpPa-1-COF heterojunction and H_2 and O_2 evolution rate of piezocatalysis. Reproduced with permission [70]. Copyright 2021, the John Wily and Sons. (b) Stress tunable dipolar ordering, redistribution of electrons and holes, and H_2 and O_2 evolution rate of piezocatalysis. Reproduced with permission [44]. Copyright 2025, the John Wily and Sons.

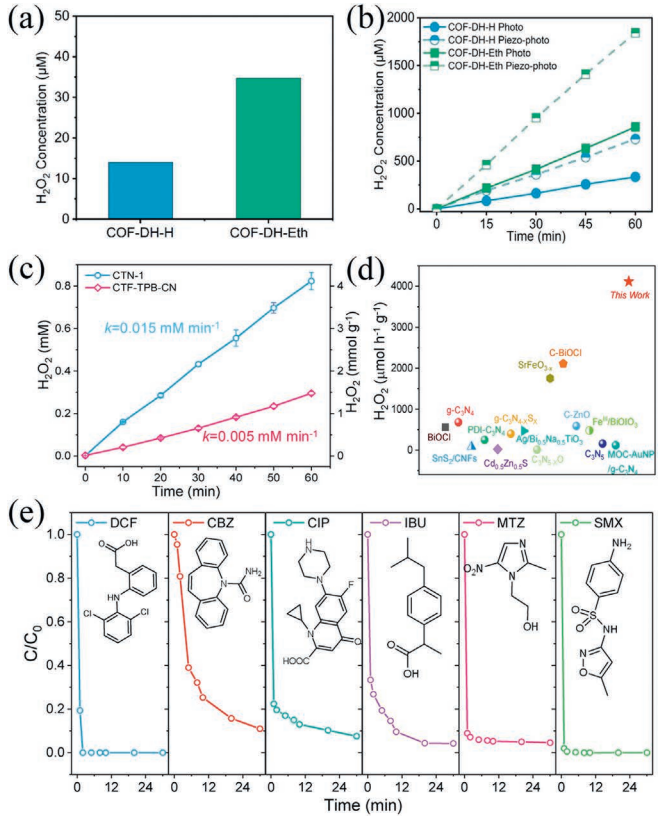


Fig. 11. (a) Piezocatalytic H_2O_2 evolution by COF-DH–H and COF-DH-Eth in 1 h (5 mg catalyst in 25 mL H_2O). (b) The Piezo-photocatalytic H_2O_2 performance of COF-DH–H and COF-DH-Eth. Reproduced with permission [42]. Copyright 2024, the John Wily and Sons. (c) Piezocatalytic H_2O_2 evolution by CTFs. (d) Performance comparison for H_2O_2 production. (e) Degradation of various pollutants using CTN-1 as piezocatalyst; Reproduced with permission [34]. Copyright 2024, the John Wily and Sons.

3.1.2. *Piezocatalytic water splitting*

The generation of H_2 and O_2 (or H_2O_2) through overall water splitting represents a highly promising technological advancement, yet it continues to pose significant challenges. In 2022, Lan and colleagues showed that TpPa-1-COF could act as a catalyst for overall water splitting with relatively low performance, achieving production rates of approximately 24 $\mu mol\,h^{-1}\,g^{-1}$ for H_2 and 12 $\mu mol\,h^{-1}\,g^{-1}$ for O_2 under ultrasonic irradiation (40 kHz, 100 W) in vacuum conditions (Fig. 10a) [70]. This is the first report on the piezocatalytic performance of COFs, although piezoelectric properties have not been studied.

EA-COF was also confirmed to exhibit piezo-catalytic activity, facilitating the overall water splitting, with 53.5 $\mu mol\ h^{-1}\,g^{-1}$ for H_2 production and 183.0 $\mu mol\ h^{-1}\,g^{-1}$ for H_2O_2 generation under ultrasound (40 kHz, 60 W), respectively [41]. The composite structures were found to significantly enhance piezocatalytic performance [71]. The metal–organic cage (MOC-Q3) was incorporated into EA-COF through supramolecular interactions, resulting in the formation of a Z-type single-atom MOC-Q3/COF composite. As expected, the Z-type MOC-Q3/EA-COF catalyst exhibited enhanced piezocatalytic performance. Further, the better overall water splitting efficiency could be obtained by the piezo-photocatalysis, with 426.4 $\mu mol\ h^{-1}\,g^{-1}$ for H_2 production and 535.1 $\mu mol\ h^{-1}\,g^{-1}$ for H_2O_2.

TAPA-PDA has good piezoelectricity and the charge transfer between TAPA and PDA subunits leads to the generation of dipoles [44]. Under external force, numerous electron-hole pairs are generated on the surface of the COF pores, which overcomes the problem of low density of electron-hole pairs available on the surface of most piezoelectric catalysts (Fig. 10b). And the pores in the COF enable water molecules to easily diffuse to the surface to touch the available charge. Further, TAPA-PDA was exfoliated into nanosheets. Thus, TAPA-PDA nanosheets (Ns) has an impressive piezocatalytic water splitting performance, with 6.6 mmol $h^{-1}\,g^{-1}$ of H_2 and 2.1 mmol $h^{-1}\,g^{-1}$ of O_2 under ultrasonic conditions (40 kHz, 200 W) [44].

3.1.3. *Piezocatalytic H_2O_2 production*

H_2O_2 is a crucial oxidizing agent and chemical intermediate, and the direct synthesis of H_2O_2 from water and air represents a green and sustainable approach to its production. Han and colleagues evaluated catalytic performance for H_2O_2 production in pure water and air [42]. Under ultrasonic conditions (40 kHz, 50 W), COF-DH–H and COF-DH-Eth exhibited minimal H_2O_2 production rates of approximately 75 and 175 $\mu mol\ g^{-1}\,h^{-1}$, respectively (Fig. 11a). Additionally, the piezocatalytic H_2O_2 generation rate for bifluorenylidene-based COFs (COF-BFTB-H) was found to be ~800 $\mu mol\ g^{-1}\,h^{-1}$. Upon visible light irradiation, COF-

DH–H demonstrated a H_2O_2 production rate of 1668 μmol g^{-1} h^{-1}, whereas COF-DH-Eth exhibited a significantly higher rate of 3840 μmol g^{-1} h^{-1}. The piezo-photocatalytic H_2O_2 generation rates of COF-DH–H and COF-DH-Eth further increased to 3656 and 9212 μmol g^{-1} h^{-1}, respectively (Fig. 11b). For comparison, COF-TAPB-PD was also synthesized for H_2O_2 production, demonstrating similar yields for both photocatalytic and piezo-photocatalytic processes. These results suggest that the enhanced performance observed during piezo-photocatalysis is related to the piezoelectric polarization field in the Cz-COFs.

Zhu *et al*. evaluated the piezocatalytic H_2O_2 production performance of SASb-TpBpy-COF under ultrasonic conditions (40 kHz, 110 W) in pure water and air [46]. SASb-TpBpy-COF, with 1.5 wt% Sb loading, exhibited a high H_2O_2 yield of 1500.6 μmol g^{-1} h^{-1}, which was much higher than that of TpBpy-COF (209.8 μmol g^{-1} h^{-1}). Moreover, the rate of H_2O_2 production decreased with decreasing Sb loading, suggesting that the 5p-2p orbital hybridized Sb single-atom is a key factor in the yield of H_2O_2 piezoelectric synthesis. The DFT calculations showed that the Sb single atoms in SASb-TpBpy-COF are intrinsically highly selective for O_2 adsorption, which leads to the rapid oxygen reduction to produce H_2O_2 by a non-radical pathway.

The high specific surface area, nitrogen-enriched structure, and fully conjugated framework of CTFs facilitate its potential for improved catalytic performance for H_2O_2 production. Under ultrasonic conditions (40 kHz, 100 W), Jin *et al*. reported the piezocatalytic H_2O_2 evolution rate by CTN-1 could be up to 4115 μmol g^{-1} h^{-1} under air and pure water [34], surpassing other piezocatalysts reported to date (Figs. 11c and d). In contrast, the CTF-TPB-CN only showed the piezocatalytic H_2O_2 generation rate with 1560 μmol g^{-1} h^{-1}. These results indicate that improving the piezoelectric response by controlling the morphology during piezocatalysis can enhance the piezocatalytic performance of the materials.

3.1.4. Piezocatalytic degradation of pollutants

Pollutant degradation has always been an important topic for human health and environmental remediation. Encouraged by the good piezocatalytic H_2O_2 production performance, Zhu *et al*. further evaluated the pollutant degradation of SASb-TpBpy-COF-based piezoelectric-Fenton system for emerging pollutants [46], including caffeine (CAF), carbamazepine (CBZ), sulfamethoxazole (SMX), acetaminophen (PCM) and naproxen (NPX). The results showed that the *in-situ* degradation efficiency of the system for pollutants exceeded 80 % in 60 min. Among them, the degradation efficiency of PCM reached 100 % within 30 min.

Jin *et al*. demonstrated the excellent piezocatalytic H_2O_2 generation rate of CTN-1, and further, they constructed a piezo-catalytic Fenton (PSF) system by adding $FeSO_4$ to degrade a variety of pollutants using CTN-1 [34]. As expected, this system showed good degradation results for a wide range of pollutants (Fig. 11e). The degradation rates of diclofenac (DCF) and sulfamethoxazole (SMX) were close to 100 % within a few minutes, and the degradation rates of metronidazole (MTZ) and ibuprofen (IBU) were about 95 %. Meanwhile, carbamazepine (CBZ) and ciprofloxacin (CIP) showed high degradation rates (about 90 %).

3.1.5. Piezocatalytic reduction of uranium

Given the rapid advancements in nuclear energy, the accumulation of radioactive uranium in natural water have been significantly intensified, posing a substantial threat to human health and the environment. Consequently, the development of highly efficient technologies for uranium removal have become a matter of critical importance. Uranium predominantly exists in aqueous environments in two oxidation states, soluble uranium(VI) and stable uranium(IV). Qiu *et al*. conducted a comprehensive evaluation of the piezocatalytic performance of the D-COF@ZnO heterojunction in the reduction of U(VI) to stable U(IV) [45]. Their experimental findings revealed that the D-COF@ZnO heterojunction exhibited optimal uranium removal efficiency at a pH value of 5, with its performance markedly surpassing that of other comparable materials (Fig. 12a). The heterojunction demonstrated the capacity to achieve adsorption equilibrium within a relatively brief timeframe, indicative of its rapid piezoelectric removal kinetics (Fig. 12b). Without sonication, all materials had only low uranium adsorption capacity (Fig. 12c). Ultimately, D-COF@ZnO achieved an exceptionally high uranium removal capacity up to 2010.65 mg/g under ultrasound (40 kHz, 120 W) (Fig. 12d). Furthermore, when tested in actual waste water, D-COF@ZnO maintained specific recognition of U(VI) ions and continued to exhibit high removal efficiency, thereby substantiating its potential applicability in practical water treatment scenarios.

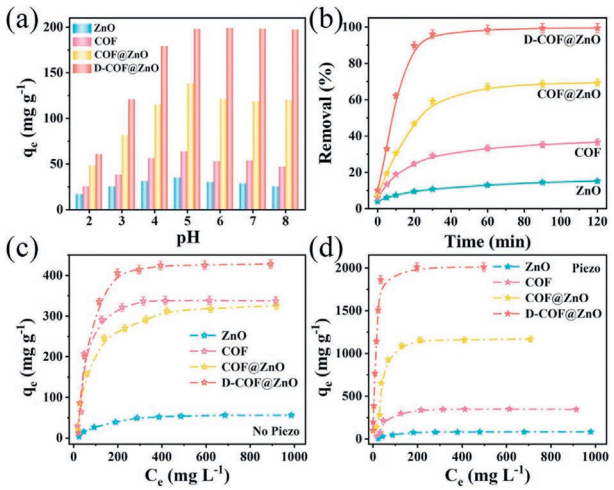


Fig. 12. (a) U(VI) removal at different pH conditions. (b) Kinetics curves of U(VI) removal under ultrasonic. (c) U(VI) removal without ultrasound and (d) U(VI) removal under ultrasound. Reproduced with permission [45]. Copyright 2024, the John Wily and Sons.

3.2. COFs for piezoelectric nanogenerators (PENGs)

Piezoelectric nanogenerators (PENGs) are devices that use piezoelectric materials to efficiently utilize mechanical energy to generate electrical energy [72–75]. As shown in Fig. 1a, the internal charge distribution in the piezoelectric material is altered, leading to the generation of surface charges and the establishment of a potential difference, which results in the generation of an electrical current. PENGs offer several advantages, including high energy conversion efficiency, a wide range of potential applications and environmental sustainability. As a result, they have attracted considerable attention for self-powered sensor networks, wearable devices, smart homes, the Internet of Things (IoT), biomedicine and other fields [76–79].

Han *et al*. synthesized piezoelectric COFs by utilizing twisted molecular structures (Fig. 3a), and subsequently developed PENGs by filling these piezoelectric materials between two silver electrodes. The resulting PENGs based on COF-DH–H and COF-DH-Eth exhibited open-circuit voltages of 2 and 6 V, respectively, when a force of 20 N was applied (Figs. 13a-c) [42]. Those performances are superior to many organic piezoelectric materials [43,80,81].

Zhang *et al*. developed PENGs based on CityU-13 and CityU-14 [35]. In brief, COFs (15 wt%) were blended into polydimethylsiloxane (PDMS), then removing bubbles, and molded as active layers in the middle of Al metal electrodes. The corresponding PENGs have high open circuit voltage outputs of 60 and 50 V (Fig. 13d). These performances are among the highest reported for PENGs

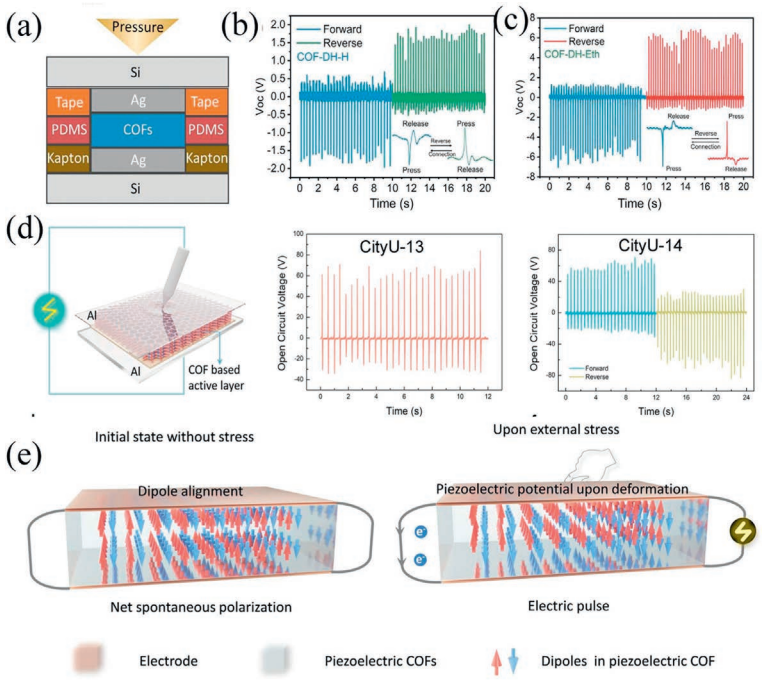


Fig. 13. (a) Schematic diagram of the piezoelectric nanogenerator; Output open-circuit voltage of PENG based on (b) COF-DH–H and (c) COF-DH-Eth tested by PENG. Reproduced with permission [42]. Copyright 2024, the John Wily and Sons. (d) Output open-circuit voltage of PENG based on CityU-13 and CityU-14. (e) Schematics of dipole alignment and net spontaneous polarization in COFs without stress and piezoelectricity with electric pulse due to positive/negative charge separation upon stress. Reproduced with permission [35]. Copyright 2024, the John Wily and Sons.

Table 1
Summary for the piezoelectric applications of COFs.

Samples	Piezoelectric coefficient	Applications	Results	Ref.
TpPa-1-COF	–	Piezocatalytic water splitting	H_2 (~24 μmol h^{-1} g^{-1}), O_2 (~12 μmol h^{-1} g^{-1})[b]	[70]
EA-COF	319.20 pm/V	Piezocatalytic water splitting	H_2 (53.5 μmol h^{-1} g^{-1}), H_2O_2 (183.0 μmol h^{-1} g^{-1})	[41]
TAPA-PDA Ns	–	Piezocatalytic water splitting	H_2 (6600 μmol h^{-1} g^{-1}), O_2 (2100 μmol h^{-1} g^{-1})	[44]
COF-DH-H	41.5 pm/V	Piezocatalytic H_2O_2 production	H_2O_2 (~75 μmol h^{-1} g^{-1})[b]	[42]
COF-DH-Eth	65.1 pm/V	Piezocatalytic H_2O_2 production	H_2O_2 (~175 μmol h^{-1} g^{-1})[b]	[42]
COF-BFTB-H	25.3 pm/V	Piezocatalytic H_2O_2 production	H_2O_2 (~800 μmol h^{-1} g^{-1})[b]	[42]
TpBpy-COF	126.3 pm/V	Piezocatalytic H_2O_2 production	H_2O_2 (209.8 μmol h^{-1} g^{-1})	[46]
SASb-TpBpy-COF	287.6 pm/V	Piezocatalytic H_2O_2 production	H_2O_2 (1500.6 μmol h^{-1} g^{-1})	[46]
CTF-TPB-CN	–	Piezocatalytic H_2O_2 production	H_2O_2 (1560 μmol h^{-1} g^{-1})	[34]
CTN-1	–	Piezocatalytic H_2O_2 production	H_2O_2 (4115 μmol h^{-1} g^{-1})	[34]
SASb-TpBpy-COF	287.6 pm/V	Piezocatalytic degradation of pollutants	Degradation efficiency>80%	[46]
CTN-1	–	Piezocatalytic degradation of pollutants	Degradation efficiency>90%	[34]
D-COF@ZnO	56.1 pm/V	Piezocatalytic reduction of uranium	Uranium removal capacity: 2010.65 mg/g	[45]
COF-DH-H	41.5 pm/V	Piezoelectric nanogenerators	Open-circuit voltages: 4V	[42]
COF-DH-Eth	65.1 pm/V	Piezoelectric nanogenerators	Open-circuit voltages: 6V	[42]
CityU-13	20.9 pC/N[a]	Piezoelectric nanogenerators	Open-circuit voltages: 60 V	[35]
CityU-14	18.9 pC/N[a]	Piezoelectric nanogenerators	Open-circuit voltages: 50 V	[35]

[a] Measured by the *quasi*-static method.
[b] Estimated value.

based on organic materials [81–83]. Under mechanical stress, the dipoles within the COFs experience spatial segregation, generating piezoelectric potentials that induce a current within the circuit (Fig. 13e). These COF-based PENGs demonstrates substantial potential as a novel piezoelectric material for self-powered systems.

In overview, COFs as a rising new type of piezoelectric materials, demonstrate excellent performance metrics in diverse applications such as piezocatalysis and energy harvesting *via* nanogenerators. Their unique structural advantages, including atomic-level designability, intrinsic porosity, and tunable polarization, make the piezoelectric properties of COFs endlessly imaginable. However, research into the piezoelectric properties of COFs is still in its early stages. Here, Table 1 is presented as a comprehensive collection of state-of-the-art piezoelectric COFs, summarizing their piezoelectric coefficients, applications and superior performance.

4. Structural evolution of COFs under pressure

The application of external forces during the operation of piezoelectric materials causes a change in the position of the atoms in the material (Fig. 1a), which has an impact on their physical and chemical properties. Therefore, an in-depth understanding of the structural evolution of materials under pressure is essential to optimize their performance, expand their application areas and ensure the success of their future practical applications.

Theoretical calculations provide a convenient way to explore how materials change under pressure. In 2018, Zhang's group reported that COFs could undergo phase transformation when subjected to compressive strain through molecular dynamics simulations and DFT calculations [84]. After the phase transformation, a significant reduction in Young's modulus and thermal conduc-

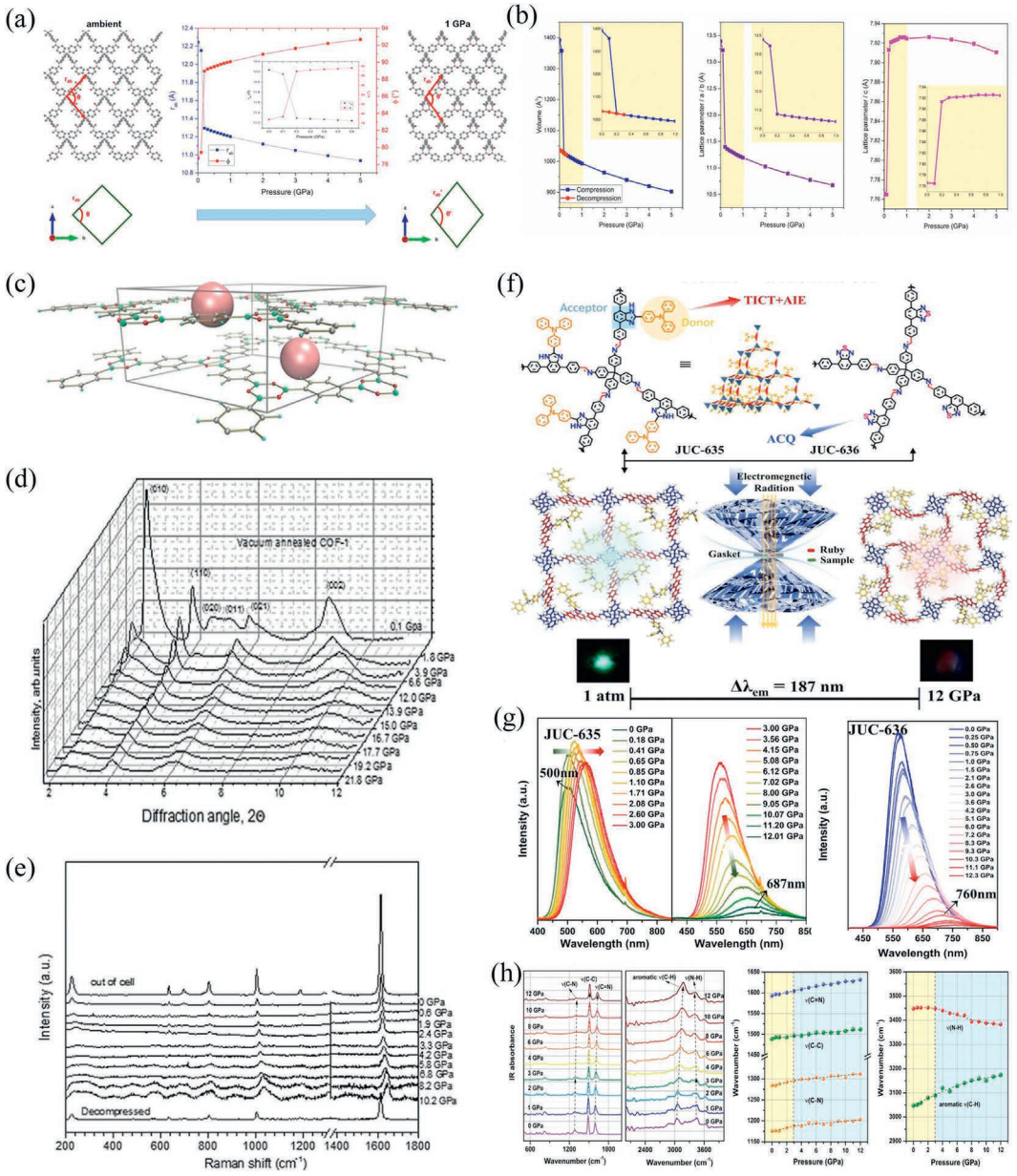


Fig. 14. (a) Changes of NPN-1 on pressure. (b) The evolution of lattice parameters in NPN-1 under compression. Reproduced with permission [85]. Copyright 2023, Elsevier. (c) Crystal structure model of COF-1-M. (d) XRD patterns of COF-1 under isotropic compression. (e) Raman spectra of COF-1under pressure. Reproduced with permission [88]. Copyright 2023, the John Wily and Sons. (f) The two 3D COFs and piezochromic behavior. (g) Fluorescence spectra of JUC-635 and JUC-636 under different pressure. (h) IR spectroscopy of JUC-635 and fitting of the IR peaks of different vibration modes. Reproduced with permission [90]. Copyright 2023, the John Wily and Sons.

tivity of the COF was observed, accompanied by a pronounced anisotropy in these properties. Notably, it was found that the phase transition had a considerable impact on the bandgap of the COF, leading to notable modifications in their semiconducting behavior. Erkartal also investigated the irreversible phase transition of the three-dimensional COF (NPN-1) under pressure using various first-principles molecular simulation (Fig. 14a) [85]. The results indicated a 27 % reduction in volume, a 15 % decrease in the cell parameters a and *b*-axis, and a 2 % expansion along the *c*-axis under a pressure of 0.2 GPa (Fig. 14b). NPN-1 adopts a strut-hinge model, which leads to an increase in the strut angle beyond the deformation of the struts under compression, thereby inducing a negative linear compressibility (NLC) phenomenon. In particular, the hinge angle rapidly grows at a rate of 13 % while the strut length falls at a rate of 7 %, providing strong evidence for the strut and hinge mechanism as the driving force behind the first-order phase transition associated to NLC. Above 0.2 GPa, the structure exhibits a decrease in compressibility, indicative of a transition to a less compressible regime (Fig. 14a). These findings elucidate the phase transition mechanisms in NPN-1 under pressure.

Advances in technology, in particular the development of the diamond anvil cell (DAC), have provided a powerful means of investigating the structural transformations of materials under high pressure conditions [86]. Common *in situ* characterization techniques include high pressure X-ray diffraction (XRD), Raman spectroscopy, infrared (IR) spectroscopy, fluorescence spectroscopy and UV–visible absorption spectroscopy [86]. These techniques can be used to monitor changes in the crystalline, chemical and electronic structures of piezoelectric materials under pressure. For example, Xiong *et al.* used pressure-dependent Raman spectroscopy to confirm structural phase transition of piezoelectric molecular crystal (HFPD) [82]. Zhu *et al.* used *in situ* UV-visible absorption

spectroscopy and fluorescence spectroscopy to explore charge migration behavior [87]. These techniques could provide a powerful window into the structural evolution of COFs during piezoelectric processes, providing critical information that could inform the design of COF-based materials for piezoelectric applications, although they may not fully replicate the specific conditions encountered in piezoelectric applications.

In 2019, Talyzin *et al.* explored the high-pressure behavior of COF-1 (Figs. 14c-e) [88]. XRD results at high pressures showed that COF-1 displays significant compressibility along the *c*-axis and lower compressibility along the *a*-axis with increasing pressure, indicating the rigid structure within the COF layers and the relatively weak π-π stacking between the layers. At pressures up to 12–15 GPa, COF-1 exhibits excellent stability and reversibly recovered after decompression (Fig. 14d). In addition, beyond the pressure range of 12–15 GPa, COF-1 undergoes an irreversible phase transition and the Raman spectrum changes drastically (Fig. 14e), with most of the peaks disappearing, which may be attributed to structural collapse. The high-pressure structural behavior of CTF-2 was studied by Popov *et al.* [89]. Their study revealed significant changes in the characteristic peaks as a function of pressure in Raman spectroscopy, implying modification of the hybridization state of the carbon atoms within the material, as well as a distortion of the triazine ring structure.

Fang and colleagues synthesized two distinct 3D COFs, named JUC-635 and JUC-636, incorporating different chromophores, and investigated their piezochromic behavior under high pressure using fluorescence spectroscopy (Fig. 14f) [90]. Upon applying pressure up to 3 GPa, JUC-635 exhibited an almost constant fluorescence intensity, accompanied by a redshift of the emission peak from 500 nm to 562 nm (Fig. 14g). Further, this framework also displayed a significant emission difference up to pressures of 12 GPa, demonstrating a better pressure sensitivity (15.58 nm/GPa) compared to many other materials. This study represents the first report of piezofluorochromism in COFs. In contrast, JUC-636 showed a rapid 51 % decrease in fluorescence intensity when subjected to a pressure of 3 GPa (Fig. 14g). The authors employed high-pressure infrared (IR) spectroscopy to explore the pressure-induced structural changes (Fig. 14h). For JUC-635, the peaks shifted to higher wavenumbers under pressure, suggesting an increase in vibrational frequencies. Among the most prominent changes were observed for the C=N stretch, indicating framework deformation. Notably, the C–N bond in TPA exhibited significant shifts from 0 to 3 GPa (3.86 cm^{-1}/GPa), with a slower progression observed between 3 and 12 GPa (1.71 cm^{-1}/GPa). Similar trends were observed for the C–H bonds, which further supported that the framework deformation of JUC-635 enhances interactions between the triphenylamine (TPA) group within the pores, restricting their rotational mobility and thereby maintaining fluorescence under pressure. When the pressure exceeded 3 GPa, the reduction in layer spacing increased the hydrogen bond formation, while the enhanced vibrational activity of other bonds contributed to a non-radiative process, which ultimately became the dominant factor leading to the observed fluorescence quenching. As evidence, the N–H peak of imidazole was red-shifted after 3 GPa, which was due to the reduction of the layer spacing, which enhanced the N–H···N hydrogen bonding between the imidazole rings. Fang *et al.* further synthesized a series of bicarbazole-based COFs to investigate the impact of topologies, dimensions, and linkages [91]. The structures and piezofluorochromism of these COFs were then investigated under high pressure. The 3D COFs, JUC-620 with *dia* topology and JUC-621 with *qtz* topology, exhibited remarkable piezo-induced enhanced emission (PIEE) phenomena, where the fluorescence intensity of JUC-620 with a dia-net increased by 16-fold, surpassing the known PIEE properties of covalent organic porous materials (CPMs) and most organic small molecules. Below 5 GPa, the

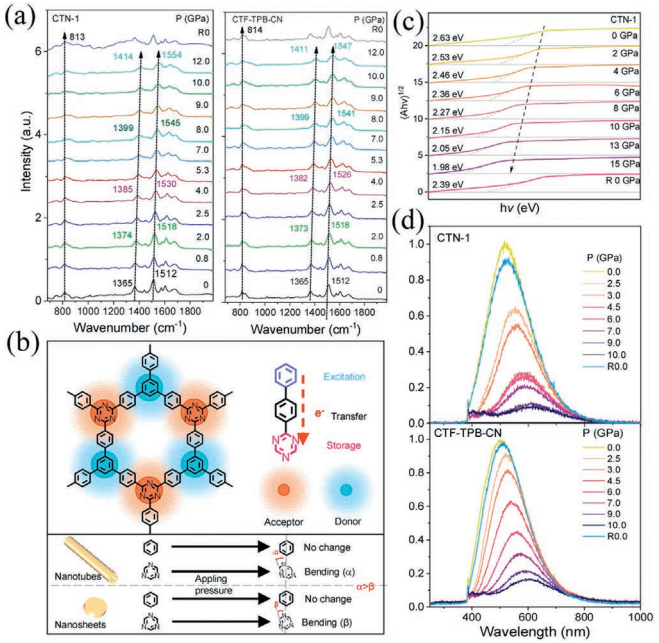


Fig. 15. (a) *In situ* IR spectroscopies of CTN-1and CTF-TPB-CN under high pressure. (b) Schematic representation of electron conduction and changes of CTFs under pressure. (c) Pressure-dependent UV-visible absorption spectroscopy. (d) Pressure-dependent fluorescence spectroscopy. Reproduced with permission [34]. Copyright 2024, the John Wily and Sons.

fluorescence intensity of JUC-621 rose by a factor of 6.7. In contrast, 2D COFs with flexible structures exhibited rare blue-shifted luminescence, whereas 2D COF typically displayed red-shifts and a reduction in fluorescence intensity. To clarify the mechanism underlying the PIEE of in 3D COFs, the authors used IR spectroscopy to record the structural evolution of COFs under pressure. The vibration of C–H bonds at around 810 cm^{-1} showed smaller shifts in the pressure range where fluorescence enhancement occurred. This suggested that the deformation vibrations of the C–H bonds were constrained by complex intramolecular interactions in this pressure range, leading to a marked increase in fluorescence. At 1 GPa pressure, the peak of C=N shows a blue shift of 6 cm^{-1} in JUC-620, whereas the peak of JUC-621 is unchanged, demonstrating that the *dia* topology is more likely to be activated by pressure than the *qtz* topology in this system.

Jin *et al.* recently investigated the structural transformations and carrier separation processes of CTFs with different morphologies under applied pressure using various high-pressure *in-situ* spectroscopic techniques [34]. *In-situ* high-pressure IR spectroscopy revealed that the two peaks attributed to the triazine rings gradually shifted with increasing pressure, while the peaks corresponding to the benzene ring remained unaffected (Fig. 15a). This observation suggests that pressure primarily induces structural changes in the triazine ring. DFT calculations further confirmed these findings, indicating that under high pressure, the bond angles within the triazine ring undergo significant changes, leading to its structural deformation (Fig. 7c). The peaks of CTN-1 showed a more pronounced blue shift compared to the bulk sample under the same pressure conditions, highlighting the increased pressure sensitivity (Figs. 15a and b). To further investigate carrier migration during catalysis, *in-situ* UV-visible absorption spectroscopy under high pressure conditions was used to monitor the redox band positions of CTFs. With increasing pressure, the band gap of CTN-1 narrowed from 2.63 eV to 1.98 eV (Fig. 15c). The reduced band gap generally facilitates charge migration. And *in situ* high-pressure fluorescence spectroscopy revealed a decrease in in-

tensity with increasing pressure from 0.0 GPa to 10 GPa, accompanied by significant red shifts in the two CTFs (Fig. 15d). These results indicate that the efficiency of charge recombination inhibition in the CTFs improves with external pressure, highlighting the enhanced charge separation efficiency in the CTF during piezoelectric catalysis. DFT calculations further revealed a significant reduction in the interlayer spacing between the layers of the CTF and a shortening of the bond length with pressure, both of which promote efficient charge separation.

5. Conclusions and outlook

COFs have garnered much attention in recent years benefiting from their intrinsic advantages, such as well-defined and ordered frameworks, conjugated structures, easy functionalization and high surface area. Despite these promising attributes, the piezoelectric properties of COFs were initially investigated. Currently, strategies such as building block design, defect engineering, and morphology control have been adopted to upgrade the piezoelectric performance of COFs, leading to notable advancements in applications such as catalysis and piezoelectric nanogenerators. There are still many issues to be developed in terms of material design, mechanism, and applications.

Although COFs exhibit high crystallinity, the presence of unidentified defects remains a challenge, and the influence of their crystal structure or intrinsic defects on piezoelectric properties requires further investigation. Recent advancements in the synthesis of single-crystal COFs have made significant progress [92–95], and research on the structure and piezoelectric properties of high-quality single-crystal COFs would be crucial in addressing this issue. Furthermore, the piezoelectric mechanisms of COF materials can be explored more comprehensively through the efficient molecular dynamic simulations and DFT calculations.

Despite the promising potential of COFs as piezoelectric materials, their piezoelectric coefficients remain relatively low compared with conventional inorganic piezoelectric materials. Enhancing the piezoelectric response of COF materials remains a significant challenge in current research. The development of COF synthesis method with milder and more universal conditions will offer greater opportunities for structural diversity and morphological modulation, thereby facilitating the identification of COFs with enhanced piezoelectric performance. Additionally, high-throughput chemistry and machine learning great opportunities for the prediction and design of novel COF materials with superior piezoelectric properties.

Although piezoelectric COFs exhibit good piezoelectric performance under laboratory conditions, their performance may be affected by environmental factors (*e.g.*, humidity, temperature) in practical applications. Therefore, further research is needed to improve the performance stability of piezoelectric COFs to ensure their reliability in long-term use. Moreover, COFs are typically used in powder form and processability remains a challenge, although some progress has been made. Therefore, composite of piezoelectric COFs with other materials for specific functions and applications are good means. However, the interaction between different materials may have an impact on the performance of piezoelectric COFs. Therefore, in-depth studies are needed to investigate the compatibility of piezoelectric COFs with other materials and how to optimize interfacial interactions to improve performance.

In terms of applications, COFs, with their high specific surface area and regular pore channels, can also be used as efficient piezoelectric sensors by introducing functional groups to improve adsorption of target analytes (*e.g.*, toxic gas molecules), causing lattice changes or shielding charges induced by external forces. Compared to other piezoelectric materials, piezoelectric COFs are lightweight and have great potential for enhanced biocompatibility, allowing them to be integrated into wearable devices as piezoelectric sensors or PENG-based self-powered sensors for real-time monitoring of human physiological signals and analyzing movement conditions. Furthermore, based on current research, COFs demonstrate promising prospects in the field of piezocatalysis, and more high value-added products are worth further exploration.

CRediT authorship contribution statement

Lijiang Guan: Writing – original draft. **Danyal Mehdi:** Data curation. **Haoxiang Li:** Writing – review & editing. **Fei Chen:** Project administration. **Shangbin Jin:** Writing – review & editing, Funding acquisition.

Declaration of competing interest

The authors declare that they have no known competing financial interests or personal relationships that could have appeared to influence the work reported in this paper.

Acknowledgments

This work had funding support from Qinchuangyuan High Level Innovation and Entrepreneurship Talent Project (No. QCYYRCXM-2022–23), Shaanxi Provincial Outstanding Youth Science Fund (No. 2025JC-JCQN 002), Aeronautical Science Foundation of China (No. 2023Z056070001), National Natural Science Foundation of China (Nos. 22275143 and 22322604) and Key Project of Natural Science Basic Research Program of Shaanxi (No. 2023JC-XJ-14).

References

[1] B. Jaffe, W.R. Cook, H. Jaffe, Chapter I - historical introduction, in: B. Jaffe, W.R. Cook, H. Jaffe (Eds.), Piezoelectric Ceramics, Academic Press, 1971, pp. 1–5.
[2] Z.L. Wang, J. Phys. Chem. Lett. 1 (2010) 1388–1393.
[3] K. Wang, C. Han, J. Li, et al., Angew. Chem. Int. Ed. 61 (2022) e202110429.
[4] J. Liu, W. Qi, M. Xu, et al., Angew. Chem. Int. Ed. 62 (2023) e202213927.
[5] K. Kapat, Q.T.H. Shubhra, M. Zhou, S. Leeuwenburgh, Adv. Funct. Mater. 30 (2020) 1909045.
[6] M. Habib, I. Lantgios, K. Hornbostel, J. Phys. D: Appl. Phys. 55 (2022) 423002.
[7] R. Bechmann, Phys. Rev. 110 (1958) 1060–1061.
[8] Q. Yang, X. Guo, W. Wang, et al., ACS Nano 4 (2010) 6285–6291.
[9] W. Wu, L. Wang, Y. Li, et al., Nature 514 (2014) 470–474.
[10] M. Acosta, N. Novak, V. Rojas, et al., Appl. Phys. Rev. 4 (2017) 041305.
[11] J. Xu, Q. Zhang, X. Gao, et al., Angew. Chem. Int. Ed. 62 (2023) e202307018.
[12] Z. He, F. Rault, M. Lewandowski, E. Mohsenzadeh, F. Salaün, Polymers 13 (2021) 174.
[13] Y. Sun, J. Gao, Y. Cheng, Y.W. Zhang, K. Zeng, J. Phys. Chem. C 123 (2019) 3122–3129.
[14] Y. Sun, Z. Hu, D. Zhao, K. Zeng, Nanoscale 9 (2017) 12163–12169.
[15] M. Zelisko, Y. Hanlumyuang, S. Yang, et al., Nat. Commun. 5 (2014) 4284.
[16] R.C. Wang, Y.C. Lin, H.C. Chen, W.Y. Lin, Nano Energy 83 (2021) 105743.
[17] Z. Ghemari, S. Belkhiri, S. Saad, J. Comput. Electron. 23 (2024) 448–455.
[18] Z. Wu, T. Cheng, Z.L. Wang, Sensors 20 (2020) 2925.
[19] T. Vijayakanth, D.J. Liptrot, E. Gazit, R. Boomishankar, C.R. Bowen, Adv. Funct. Mater. 32 (2022) 2109492.
[20] J. Li, Y. Long, F. Yang, X. Wang, Curr. Opin. Solid State Mater. Sci. 24 (2020) 100806.
[21] X. Yuan, J. Shi, Y. Kang, et al., Adv. Mater. 36 (2023) 2308726.
[22] M. Shehzad, S. Wang, Y. Wang, Npj Flex. Electron. 5 (2021) 24.
[23] S.D. Mahapatra, P.C. Mohapatra, A.I. Aria, et al., Adv. Sci. 8 (2021) 2100864.
[24] B. Liu, X. Liu, Y. Li, et al., Eco Environ. Health. 3 (2024) 418–424.
[25] N. Meng, W. Liu, R. Jiang, et al., Prog. Mater. Sci. 138 (2023) 101161.
[26] W. Wu, Z.L. Wang, Nat. Rev. Mater. 1 (2016) 16031.
[27] A.P. Côté, A.I. Benin, N.W. Ockwig, et al., Science 310 (2005) 1166–1170.
[28] S. Kandambeth, K. Dey, R. Banerjee, J. Am. Chem. Soc. 141 (2019) 1807–1822.
[29] X. Feng, X. Ding, D. Jiang, Chem. Soc. Rev. 41 (2012) 6010–6022.
[30] W. Zhang, L. Chen, S. Dai, et al., Nature 604 (2022) 72–79.
[31] K. Geng, T. He, R. Liu, et al., Chem. Rev. 120 (2020) 8814–8933.
[32] H. Xiang, B. Xu, Y. Xia, J. Yin, Z. Liu, J. Appl. Phys. 121 (2017) 225112.
[33] M. Yan, Z. Xiao, J. Ye, et al., Energy Environ. Sci. 14 (2021) 6158–6190.
[34] L. Guan, Z. Li, K. Wang, et al., Angew. Chem. Int. Ed. 64 (2025) e202419867.
[35] Q. Gu, X. Lu, C. Chen, et al., Angew. Chem. Int. Ed. 63 (2024) e202409708.
[36] S. Ge, K. Wei, W. Peng, et al., Chem. Soc. Rev. 53 (2024) 11259–11302.
[37] K.S. Ramadan, D. Sameoto, S. Evoy, Smart Mater. Struct. 23 (2014) 033001.
[38] H. Li, C. Tian, Z.D. Deng, Appl. Phys. Rev. 1 (2014) 041301.

[39] H. Jin, X. Gao, K. Ren, et al., IEEE Trans. Ultrason. Ferroelectr. Freq. Control. 69 (2022) 3057–3069.
[40] L. Huang, S. Lin, Z. Xu, et al., Adv. Mater. 32 (2019) 1902034.
[41] Z.Z. Liang, X.A. Li, Q.Z. Chen, et al., ACS Catal. 14 (2024) 10447–10461.
[42] Z. Li, Z. Dong, Z. Zhang, et al., Angew. Chem. Int. Ed. 64 (2024) e202420218.
[43] S. Bera, S. Guerin, H. Yuan, et al., Nat. Commun. 12 (2021) 2634.
[44] A. Ghosh, S. Menon, S. Biswas, et al., Adv. Funct. Mater. 35 (2025) 2502787.
[45] J.X. Qi, J.W. Gong, Z.H. Peng, et al., Small 21 (2024) 2409682.
[46] Y. Jiao, Q. Lian, Z. Li, et al., Adv. Funct. Mater. 35 (2025) 2500501.
[47] K.S. Hong, H. Xu, H. Konishi, X. Li, J. Phys. Chem. Lett. 1 (2010) 997–1002.
[48] C. Hu, J. Hu, Z. Zhu, et al., Angew. Chem. Int. Ed. 61 (2022) e202212397.
[49] C. Wang, C. Hu, F. Chen, et al., Adv. Funct. Mater. 33 (2023) 2301144.
[50] Y. Zhang, K. Feng, M. Song, et al., Energy Environ. Sci. 18 (2025) 602–612.
[51] M. Fu, J. Luo, B. Shi, et al., Angew. Chem. Int. Ed. 63 (2023) e202316346.
[52] Y. Wen, W. Liu, P. Wang, et al., Adv. Funct. Mater. 33 (2023) 2308084.
[53] W. Liu, P. Fu, Y. Zhang, et al., Proc. Natl. Acad. Sci. U. S. A. 120 (2023) e2218813120.
[54] W. Tian, N. Li, D. Chen, et al., Angew. Chem. Int. Ed. 62 (2023) e202306964.
[55] Z. Ren, F. Chen, Q. Zhao, et al., Appl. Catal. B: Environ. 320 (2023) 122007.
[56] F. Peng, J. Lin, H. Li, et al., Nano Energy 95 (2022) 107020.
[57] X. Ning, A. Hao, X. Qiu, Adv. Funct. Mater. 35 (2024) 2413217.
[58] Z. Ren, Y. Peng, H. He, et al., Chin. J. Chem. 41 (2022) 111–128.
[59] K. Kubota, Y.D. Pang, A. Miura, H. Ito, Science 366 (2019) 1500–1504.
[60] X. Wang, X. Zhang, L. Xue, et al., Angew. Chem. Int. Ed. 62 (2023) e202307054.
[61] Y. Zhi, Z. Wang, H.L. Zhang, Q. Zhang, Small 16 (2020) 2001070.
[62] B. Mishra, A. Alam, A. Chakraborty, et al., Adv. Mater. 37 (2025) 2413118.
[63] R. Wang, Z. Zhang, H. Zhou, et al., Angew. Chem. Int. Ed. 63 (2024) e202410417.
[64] Y. Li, Z. Li, X. Lin, H. Lv, M. Zhu, Chem. Commun. 59 (2023) 5749–5752.
[65] K. Wang, D. Shao, L. Zhang, et al., J. Mater. Chem. A 7 (2019) 20383–20389.
[66] K. Wang, C. Han, Z. Shao, et al., Adv. Funct. Mater. 31 (2021) 2102089.
[67] S. Tu, Y. Guo, Y. Zhang, et al., Adv. Funct. Mater. 30 (2020) 2005158.
[68] F. Bößl, V.C. Menzel, K. Jeronimo, et al., Electrochim. Acta 462 (2023) 142730.
[69] J. He, Z. Li, P. Feng, et al., Angew. Chem. Int. Ed. 63 (2024) e202410381.
[70] M.L. Xu, M. Lu, G.Y. Qin, et al., Angew. Chem. Int. Ed. 61 (2022) e202210700.
[71] K. Cai, H. Huang, Y. Xu, et al., Nano Energy 130 (2024) 110090.
[72] H. Askari, A. Khajepour, M.B. Khamesee, Z. Saadatnia, Z.L. Wang, Nano Today 22 (2018) 10–13.
[73] J. Briscoe, N. Jalali, P. Woolliams, et al., Energy Environ. Sci. 6 (2013) 3035–3045.
[74] L. Lu, W. Ding, J. Liu, B. Yang, Nano Energy 78 (2020) 105251.
[75] H. Ryu, H.J. Yoon, S.W. Kim, Adv. Mater. 31 (2019) 1802898.
[76] K. Meng, X. Xiao, W. Wei, et al., Adv. Mater. 34 (2022) 2109357.
[77] F.R. Fan, W. Tang, Z.L. Wang, Adv. Mater. 28 (2016) 4283–4305.
[78] X. Cao, Y. Xiong, J. Sun, et al., Adv. Funct. Mater. 31 (2021) 2102983.
[79] W. Deng, Y. Zhou, A. Libanori, et al., Chem. Soc. Rev. 51 (2022) 3380–3435.
[80] S. Paul, S. Barman, A. Pal, et al., Chem. Mater. 35 (2023) 6463–6471.
[81] S. Guerin, A. Stapleton, D. Chovan, et al., Nat. Mater. 17 (2017) 180–186.
[82] H.Y. Zhang, Y.Y. Tang, Z.X. Gu, et al., Science 383 (2024) 1492–1498.
[83] W. Ji, B. Xue, Y. Yin, et al., J. Am. Chem. Soc. 144 (2022) 18375–18386.
[84] J. Zhang, Phys. Chem. Chem. Phys. 20 (2018) 29462–29471.
[85] M. Erkartal, Comput. Mater. Sci. 227 (2023) 112275.
[86] Y. Wang, Y. Yang, X. Yang, B. Zou, Sci. China Chem. 67 (2024) 2890–2903.
[87] Z. Li, Y. Zhou, Y. Zhou, et al., Nat. Commun. 14 (2023) 5742.
[88] J. Sun, A. Iakunkov, I.A. Baburin, et al., Angew. Chem. Int. Ed. 59 (2019) 1087–1092.
[89] F. Khorobrykh, K. Bulatov, I. Kutuza, et al., Mater. Chem. Phys. 308 (2023) 128312.
[90] J. Fang, Z. Fu, X. Chen, et al., Angew. Chem. Int. Ed. 62 (2023) e202304234.
[91] J. Fang, X. Yu, Y. Liu, et al., Angew. Chem. Int. Ed. 63 (2024) e202409099.
[92] J. Han, J. Feng, J. Kang, et al., Science 383 (2024) 1014–1019.
[93] L. Yi, Y. Gao, S. Luo, T. Wang, H. Deng, J. Am. Chem. Soc. 146 (2024) 19643–19648.
[94] S. Li, S. Xu, E. Lin, et al., Nat. Chem. 17 (2025) 226–232.
[95] L. Deng, W. Chen, G. Zhou, et al., J. Am. Chem. Soc. 146 (2024) 35427–35437.